Catalytic performance of dioxide reforming of methane over Co/AC-N catalysts: Effect of nitrogen doping content and calcination temperature

Yinghui Sun [a], Guojie Zhang [a,b,*], Ying Xu [a], Riguang Zhang [a]

[a] *Key Laboratory of Coal Science and Technology, Ministry of Education and Shanxi Province, Taiyuan University of Technology, Taiyuan, 030024, Shanxi, PR China*
[b] *College of Chemical Engineering, Qingdao University of Science and Technology, 53 Zhengzhou Road, Qingdao 266042, PR China*

ARTICLE INFO

ABSTRACT

The nitrogen doped activated carbon (AC-N) has been successfully prepared with commercial activated carbon as carbon material followed by a simple N-doping method using melamine as nitrogen sources. Using AC-N as the supports, cobalt supported on N-doped activated carbon (Co/AC-N) were developed and used as catalyst for dry reforming reaction (DRM). It was discovered that the Co/AC-N catalysts revealed much higher catalytic performance for DRM reaction in comparison to activated carbon supported cobalt catalyst (Co/AC). Moreover, the catalytic activity was influenced by preparation conditions of AC-N such as calcination temperature and the doping amount of nitrogen. The catalysts were characterized by BET, XRD, XPS, H_2-TPR, Raman spectroscopy and TEM. It was found that catalytic activities of the catalysts with different calcination temperature and nitrogen doping were influenced by catalyst surface defects and disorders, Co^{2+}/Co^{3+} molar ratio, the content of nitrogen function groups (graphitic N, pyrrolic-N and pyridinic-N) and interaction between active metal and support. The Raman spectroscopy illustrated that the N-doped catalyst surface defects and disorders increased, which improved the performances of the Redox catalysts. The XPS valence band also revealed that higher Co^{2+}/Co^{3+} molar ratio and nitrogen function groups was achieved by decreasing calcination temperature and increasing nitrogen doping. In short, the doping of nitrogen increased the structural defects and the interaction between active metals and supports, modified the surface electronic structure, which were facilitated the oxidation and reduction of methane and carbon dioxide.

© 2019 Hydrogen Energy Publications LLC. Published by Elsevier Ltd. All rights reserved.

Introduction

Global warming has become more serious because of the emission of greenhouse gas, which appears as one of the greatest challenges we have to face in the world [1]. Many responses such as CO_2 utilization and capture technologies [2,3] can help to reduce the content of greenhouse gas. Meanwhile, the main components of coke oven gas [4] CH_4 is

also a kind of greenhouse and the release of it causes great attention of human.

In recent years, various transformation technologies are proposed to use both greenhouse gases to get valuable chemical products. Dry reforming of methane (DRM) reaction is one of effective transformation methods to use CH_4 and CO_2 to produce syngas. Additionally, the H_2/CO molar ratio products are close to 1 and it is appropriate for valued-added chemical productions through Fischer-Tropsch (FT) process [5].

A series of metal catalysts, such as Ni, Co and Fe catalysts, have proven to have high catalytic activity for the DRM [6–8]. Among these metals, the Co-based catalysts showed excellent catalytic activity. Due to the difference in carbon deposition behavior from Ni-based catalysts and higher oxygen affinity, Co-based catalysts also be used as a potential catalyst for DRM reaction [9–11]. Moreover, many reports have demonstrated that Co-based catalysts showed lower water-gas shift (WGS) activity [12,13].

Several variables, such as support, modification method of support, promoter and preparation method can also affect that the catalytic performance [14–16]. The type of support has great influence on catalytic performance. Carbon materials, such as activated carbon (AC) [17,18], carbon nanotubes (CNTs) [19,20], carbon nanofibers (CNF) [21,22], etc., are promising supports, because of its large surface area and high stability. However, most carbon materials are chemically inert. Doping carbon materials with heteroatoms such as N and S can effectively enhance surface defects and functional groups [23–26]. Doping carbon materials with N, which are able to enhance electron mobility and modify electron density of C neighboring the nitrogen doped atoms [27,28]. In addition, it is well known that the basicity of catalyst is improved by introducing nitrogenous groups onto carbon surface.

There are two main ways to introduce N in active materials: 1) pyrolyzing N-containing precursors such as glucosamine [29], melamine resin [30,31] and polyurethane [32,33] to obtain N-doped carbon materials; 2) using N-containing compounds such as melamine [34,35], NH_3 [36,37] and urea [38,39] to modify carbon materials. There are three main kinds of nitrogenous functional group (pyridinic N, pyrrolic N, quaternary N) in N-doped catalysts. Previous studies have shown that pyridinic-N and pyrrolic-N have good activity for redox reaction [40–42]. The nitrogen atoms overlap with carbon atoms on pyridine ring to form a σ bond with sp^2 hybridized orbitals. The Pyridinic N can increase the electronic density near the Fermi level, thus the valence band structure of carbon materials can be effectively improved by Pyridinic N [43,44]. The carbon atoms and nitrogen atom of pyrrole ring are hybrid sp^2, nitrogen atom provide two p electrons to the pyrrole ring. Pyridinic N and pyrrolic N with lone-pair electrons are main Lewis basic sites for N-doped carbon materials, these basic sites have an extensive potential for ORR [45,46]. Moreover, nitrogen sources and preparation conditions have great influence on the type and content of nitrogen functional groups. Liu et al. [47] has studied the influence of calcination temperature on Fe–N-doped porous carbon catalyst activity for oxygen reduction reaction. The highest catalytic performance was achieved on the catalyst calcined at 900 °C due to the excellent surface structure and higher content of pyridinic

N. Liu et al. [48] has investigated the influence of melamine amount on the morphology of N-doped carbon nanotubes. It demonstrated that the election transfer between valence and conduction bands has greatly improve when the melamine concentration increased.

Although a considerable amount of research has been carried out on the N-doped carbon materials for electrochemical reactions, the catalytic performance of N-doped activated carbon-supported cobalt for DRM reaction has not been studied specifically so far. As known, the N-doped carbon materials could lead to greatly improvement of the redox potential. Here, we report on the development of a series of activated carbon catalysts doped with nitrogen and supported cobalt for DRM reaction. The effect of the nitrogen doping, the presence of nitrogenous functional groups and valence state of cobalt in the catalysts was investigated. We will show that the activity is significantly improved doping with nitrogen. Additionally, the influence of the calcination temperature and the doping amount of nitrogen on catalysts activity was investigated.

Experimental

Catalyst preparation

The coal based activated carbon employed in study was purchased from Xinhua Activated Carbon Factory, China. It was crushed into particles and used as support with the average size of about 0.83–0.88 mm. The nitrogen doping AC (AC-N) was prepared by melamine amination treatment route. Typically, 20 g AC was placed in beaker with 13.3 g of melamine, which was obtained from Aladdin Industrial Corporation (Shanghai, China.) dissolved in 70 mL of 80% alcohol-water solution. The homogeneous mixture was heated up form room temperature to 60 °C under continuously stirring for 5 h, followed by evaporating and drying under 110 °C for 24 h. The dried samples were heat-treated at target temperature (650, 750 and 850 °C), with a ramp of 5 °C/min and calcined in the tube furnace with a nitrogen flow rate of 100 sccm for 2 h. Finally, the samples were cooled to room temperature and used as supports. The modified AC were designated as AC-N-T (where T represents the calcination temperature). A series of catalysts with different calcination temperature were prepared as follows. In brief, the AC-N was placed in an aqueous $Co(NO_3)_2 \cdot 6H_2O$ (from Aladdin) solution with constantly stirring for 5 h. After the impregnation, the samples were filtered and dried at 105 °C in vacuum drying oven for 24 h, and then calcined at different temperature (5 °C/min ramp rate from room temperature) for 2 h in nitrogen atmosphere.

For further study of the influence of dopant concentrations on the catalytic activity. A series of different nitrogen content catalysts were prepared by the same method as above. The adding quantity of the melamine was different (13.3, 8.86 and 4.43 g), all of the modified supports were calcined at 650 °C. The prepared catalysts were denoted as Co/AC-N-M (where M represents the addition of melamine). The Co/AC catalyst without modification was prepared and used for comparison.

Catalyst characterization

N_2 adsorption-desorption experiments of all samples were conducted by on a constant volume adsorption apparatus (Beishide Instrument-ST (Beijing) Co., Ltd). All the samples were outgassed in vacuum at 250 °C under a flow of N_2 for 240 min before physisorption measurements. The pore size distribution and the pore diameter of micropore were determined by the Density Functional Theory model. The total pore volume of the catalysts was calculated from the volume of N_2 adsorption at P/P_0 of 0.99.

Bruker D8 instrument was used in transmission mode to examined the XRD patterns of calcined samples. The instrument was operated in high-throughput mode and was equipped with a Cu-Kα radiation.

X-ray photoelectron spectroscopy (XPS) analyses were conducted on a Thermo ESCALAB 250 spectrometer, using Al-Kα (1486.6 eV) X-ray source. The graphitic C1s signal at 284.8 eV was used as internal standard to correct possible deviations caused by the catalyst electric charging. The deconvolution and integration of signals was conducted by the Multipak software.

H_2-TPR of samples were collected in Micromeritics AutoChem 2920 instrument equipped with TCD detector to record H_2 consumption. Each fresh sample were loaded at the bottom of U-shape reactor. Before reduction, the sample was outgassed at 300 °C for 30 min in an argon stream, and then the sample was cooled to 30 °C, the reductant gas 10% H_2–Ar (30 mL/min) was introduced and the TPR began from 30 °C to 900 °C with a ramp of 10 °C/min.

Raman spectra were measured with Horiba Scientific instrument with an excitation-beam wavelength of 532 nm in the extended range of 100–1000 cm^{-1}. The active species distributions of the samples were carried out by using a TEM apparatus (Philips GM200).

Catalytic activity test

The catalytic performances of the samples for DRM reaction were carried out in a continuous-flow system using a fixed-bed quartz tube reactor (I.D. = 25 mm) at atmospheric pressure. For each reaction 10 g catalyst was used, and the reactant gas stream included 60 mL/min CH4 and 60 mL/min CO2 was introduced into the reactor. The contents of effluent gas from reactor were analyzed by using GC-950 (Shanghai Haixin Instrument) equipped with two molecular sieve columns. In this study, the conversions of CH4 and CO2 (X_{CH_4} and X_{CO_2}) were calculated using the following formulas:

$$X_{CH_4} = (1 - \frac{F_{out} \cdot C_{CH_4,out}}{F_{in} \cdot C_{CH_4,in}}) \times 100\%$$

$$X_{CO_2} = (1 - \frac{F_{out} \cdot C_{CO_2,out}}{F_{in} \cdot C_{CO_2,in}}) \times 100\%$$

Results and discussion

Characterization of catalysts

Fig. 1a displays N_2-adsorption-desorption isotherms of the catalysts at different calcining temperatures. All the catalysts
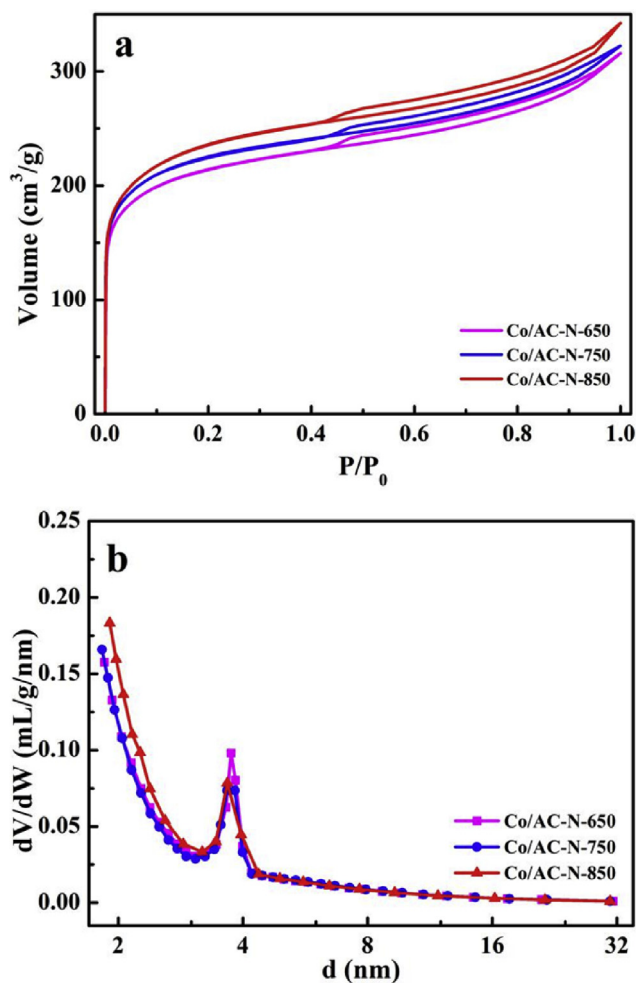

Fig. 1 – N_2-adsorption-desorption isotherms and pore size distribution of catalysts at different calcining temperatures.

show type I isotherm with a H4 hysteresis loop that sharply increases at low pressure followed by a slow increase at half way, demonstrating the micropore structure. The hysteresis loop for all catalysts are similar, Co/AC-N-850 has broader hysteresis loop than the other two, demonstrating a higher calcination temperature would lead to larger specific surface area and pore volume. Texture parameters of the catalysts are shown in Table 1, it can be seen that the specific surface area and pore volume of the catalysts slightly increased with the increase of calcination temperature. Fig. 1b shows the pore size distribution of catalysts, all the catalysts hold large number of micro-pores with the size less than 2 nm. There is a peak between 3 and 4 nm for every catalyst, which indicates that the existence of a small amount of mesoporous. It can be seen that the micropores size slightly decreases with the decrease of calcination temperature.

The XRD patterns of Co/AC-N-650, Co/AC-N-750 and Co/AC-N-850 are shown in Fig. 2. It is observed that all samples have a strong peak at $2\theta = 26.6°$, which correspond to the carbon (PDF-#26–1076). The diffraction peaks appear at $2\theta = 42.4$ and $36.4°$ are attributed to CoO phase (PDF-#43–1004). Moreover, the peak of Co_2O_3 (PDF-#02–0770) and

Table 1 — Texture parameters of the samples.

Sample	N₂ adsorption over supports		
	BET surface area (m²/g)[a]	Average pore diameter (nm)[b]	Pore volume (cm³/g)[c]
Co/AC-N-650	727.2	2.69	0.49
Co/AC-N-750	765.5	2.61	0.50
Co/AC-N-850	770.1	2.75	0.52

[a] BET specific area.
[b] Average pore diameter calculated by BJH method.
[c] Total pore volumes were obtained at $P/P_0 = 0.99$.

Co_3O_4 (PDF-#43—1003) are detected in the XRD patterns of all samples. Moreover, the peak at 60.02° corresponds to the SiC (PDF-#22—1316), this mainly due to the activated carbon which was prepared from coal.

The XPS analysis was used to determine the chemical composition and state of the N-doped catalysts. Fig. 3a shows the full XPS spectrum of three catalysts, it can be seen that the N-doped catalysts mainly composed of C, N, O and Co elements. Peaks centered at around 400 and 800 eV for all catalysts correspond to N1s and Co2p, respectively. The existence of N 1s peak in all catalysts demonstrated that N atoms were successfully doped into activated carbon support catalysts. Moreover, the XPS element analysis shows the content of N elements are 8.61%, 7.58% and 7.17% in N-doped catalysts calcined at 650, 750 and 850 °C, respectively.

The XPS spectrum of Co 2p in the Co/AC-N catalyst with various calcination temperature is shown in Fig. 3b. According to the precious studies [49,50], the XPS experimental data and peak deconvolution indicate that six peaks could fit well for Co 2p peak, which correspond to the Co^{2+} satellite, Co^{2+} and Co^{3+}. The generation of satellite peak are attributed to the energy levels splitting of Co, and it is used to confirm the existence of Co^{2+}. The Co^{2+} satellite/Co^{3+} and Co^{2+}/Co^{3+} ratio have shown in Table 2, which were obtained by the peak fitting. However, the Co^{3+} species were not observed for Co $2p_{3/2}$ on the surface of these catalysts. As shown in Fig. 3b, two
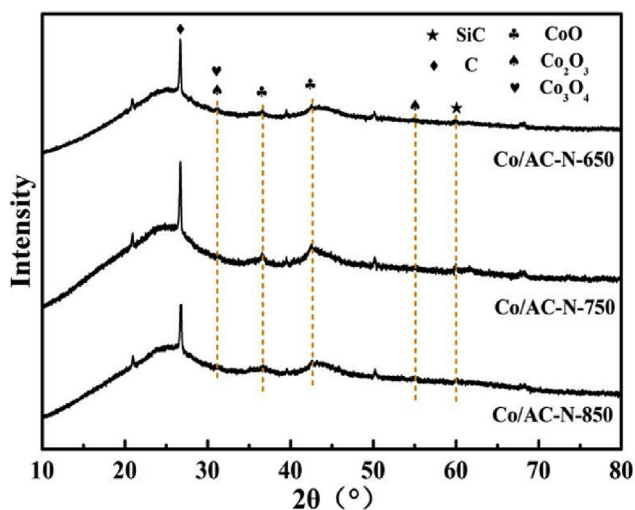
Fig. 2 — XRD patterns of Co/AC-N-650, Co/AC-N-750 and Co/AC-N-850.
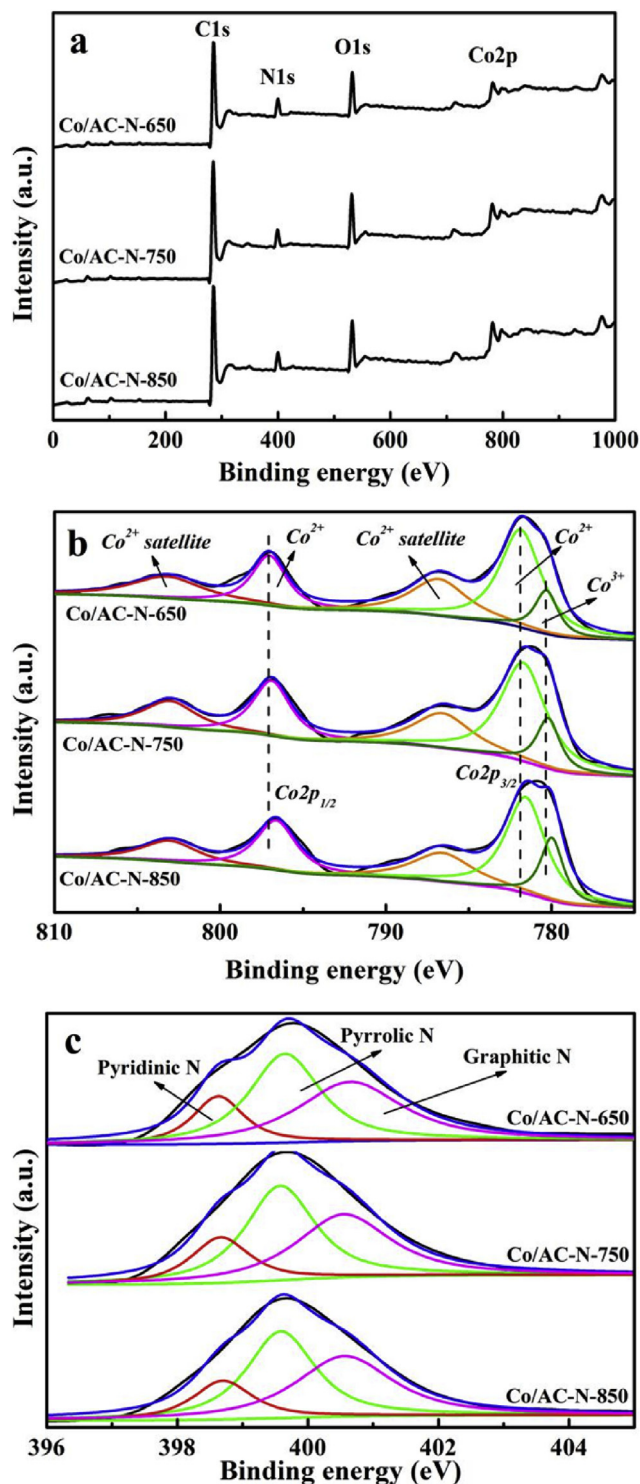
Fig. 3 — (a) XPS survey, (b) Co 2p scan and (c) N 1s scan of Co/AC-N-650, Co/AC-N-750, Co/AC-N-850.

peaks at 780.3 and 781.8 eV in the Co $2p_{3/2}$ XPS spectrum of Co/AC-N-650, which are attributed to Co^{3+} and Co^{2+}. Co^0 species were not detected by XPS analysis, which is consistent with the XRD analysis. Compared with Co $2p_{3/2}$ the XPS spectrum of Co/AC-N-650, the binding energy of Co^{3+} and Co^{2+} shifted to lower energy when the calcination temperature reached 750 and 850 °C. It was noticed that the Co^{2+}/Co^{3+} ratio decreased

Table 2 − XPS data of Co2p region for the Co/AC-N-650, Co/AC-N-750, Co/AC-N-850 catalysts.

Catalyst	Binding energy Co $2p_{1/2}$ (eV)[a]			Binding energy Co $2p_{3/2}$ (eV)[a]			Co^{2+}/Co^{3+} (molar ratio)[b]	Co^{2+} satellite/Co^{3+} (molar ratio)[b]
	Co^{2+} satellite	Co^{2+}	Co^{3+}	Co^{2+} satellite	Co^{2+}	Co^{3+}		
Co/AC-N-650	803.18(5424)	797.02(6216)	794.6(0)	786.79(7288)	781.85(14451)	780.30(3629)	5.69	3.50
Co/AC-N-750	803.01(5214)	796.87(7886)	794.3(0)	786.57(7655)	781.69(16930)	780.18(4502)	5.51	2.85
Co/AC-N-850	803.03(6005)	796.60(9995)	794.6(0)	786.57(8700)	781.56(19361)	779.98(7283)	4.03	2.02

[a] The peak area of different cobalt species.
[b] The molar ratio of Co^{2+}/Co^{3+} and Co^{2+} satellite/Co^{3+} was calculated from peak area in Fig. 4b.

with the increase of calcination temperature. It was suggested that electron transfer was happened and some of the Co^{2+} converted into Co^{3+} when the calcination temperature increased. As shown in Fig. 3c, the N 1s spectra was well fitted into three peaks, which correspond to pyrrolic-N, pyridinic-N and quaternary-N [40,43,51], all three types of nitrogenous functional groups were detected in the three catalyst. For three catalysts, pyridinic-N and graphitic N are main groups, which take up more than 80% of the total nitrogenous functional groups. More graphitic N was doped in the catalysts, increasing from 40.37 to 42.59% along with the increase of calcination temperature. However, the increase of calcination temperature causes the decrease of the content of pyrrolic-N and pyridinic-N. This contributed to the higher thermal stability of graphitic N than pyrrolic-N and pyridinic-N. The increase in calcination temperature also leaded to the decrease of the content of N atom. Moreover, the ratio decreases of the Co^{2+} satellite/Co^{3+} and Co^{2+}/Co^{3+} suggesting that the doping of N enhance the catalytic reducibility. H_2-TPR analysis results of the calcinated Co/AC-N-650, Co/AC-N-750 and Co/AC-N-850 samples are presented in Fig. 4. It can be found that two main peaks (peak α in the range of 300−500 °C and peak β in the range of 500−800 °C) is found for all N-doped catalysts. The peak α is attributed to the reduction of high dispersion Co_3O_4 to CoO and the peak β is attributed to the reduction of CoO to Co^0, which strongly interact with the N-doped supports [15,52−54]. The reduction of Co_3O_4 to CoO (peak α) produced quickly to generate a broad profile, which indicated there were
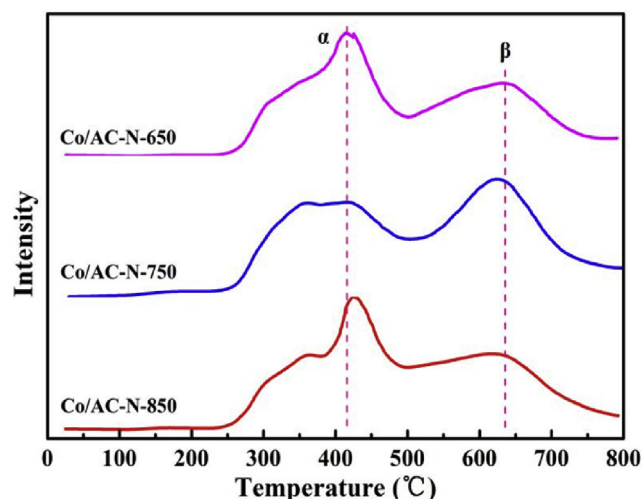
many homogeneous particle sizes of Co_3O_4 and different types of interaction between active metal and support [55]. The difference of calcination temperature does not significantly affect the H_2-TPR profiles. However, a shift of the peak α and peak β towards lower temperature is presented for three catalysts with the increase of calcination temperature, indicating that much stronger interaction of Co species with the support at lower calcination temperatures.

The Raman spectra of Co/AC-N-650, Co/AC-N-750 and Co/AC-N-850 were obtained to further study the graphitization degrees of the catalysts. In the case of Raman spectra (Fig. 5), two peaks can be ascribed to the D-band and G-band, respectively. The D band centered at 1345 cm^{-1} corresponding to the disordered carbon and G-band centered at 1580 cm^{-1} corresponding to the graphite with a higher degree of ordered carbon. The disordered carbon structures of the catalysts are obtained by the ratio of the G-band and D-band (I_D/I_G). It can be seen that, all the N-doped catalysts display high ratios of I_D/I_G, indicating the generation of more defective sites and orders, which can be attributed to the introduction of N. Compared with Co/AC-N-750 and Co/AC-N-850 (1.73 and 1.60), Co/AC-N-650 has the highest intensity ratio (2.49). The result indicates more defects and disorders were formed at low calcination temperature. Moreover, similar positions of the D and G bands and no other peaks were detected for all catalysts, which indicates that no new structure were generated.

Fig. 6 shows the $CH_4−CO_2$ reforming activities of Co/AC-N-650, Co/AC-N-750, Co/AC-N-850 at different reaction temperature. The experiments were carried out from 650 °C to 900 °C

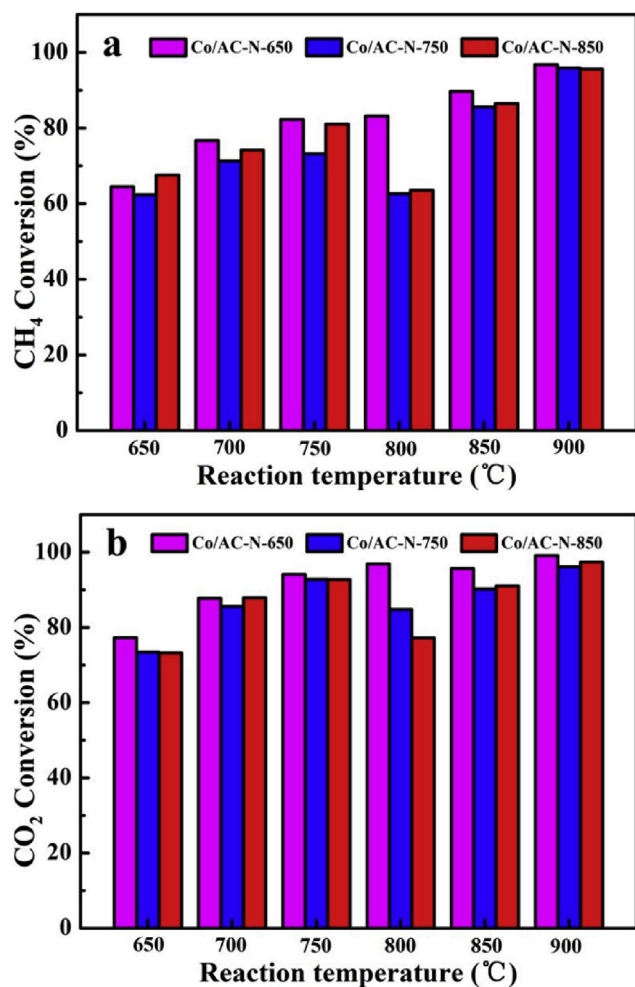Fig. 4 − H_2-TPR profile of Co/AC-N-650, Co/AC-N-750, Co/AC-N-850.
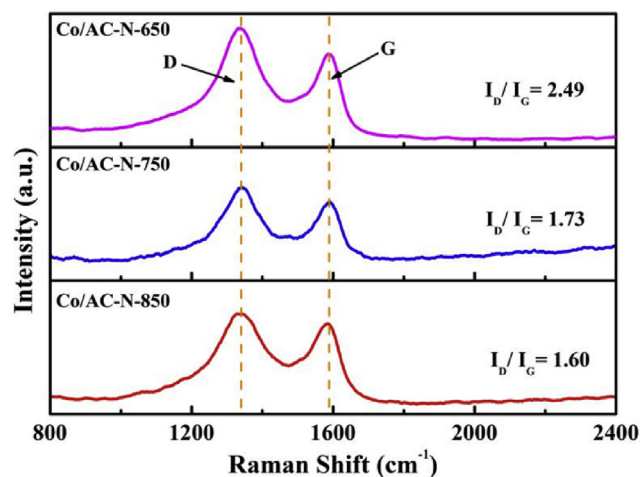
Fig. 5 − Raman spectra of Co/AC-N-650, Co/AC-N-750, Co/AC-N-850.

Fig. 6 – CH_4 (a) and CO_2 (b) conversion of Co/AC-N-650, Co/AC-N-750, Co/AC-N-850 at different reaction temperature.
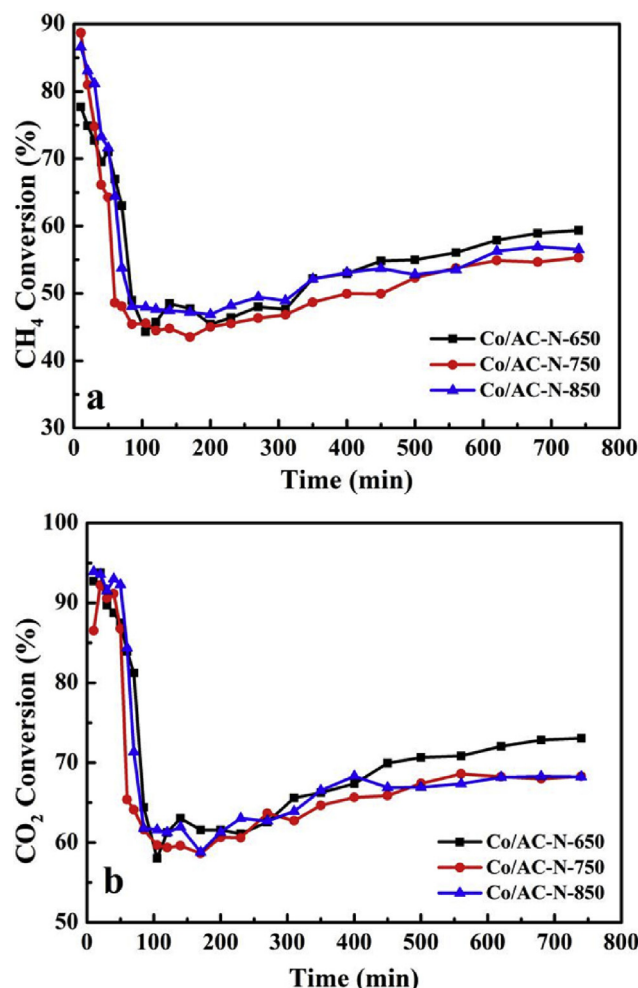

Fig. 7 – Stability tests at 800 °C: CH_4 (a) and CO_2 (b) conversion over the catalysts calcined with different temperature. Reaction conditions: $CH_4/CO_2 = 1:1$, total flow rate = 120 mL/min, 1 atm.

with CH_4: $CO_2 = 1:1$ and the flow rate of mixed gas was 120 mL/min. At each temperature, the reaction maintained for 30 min. The CH_4 and CO_2 conversion were evaluated on the basis of average values. The CH_4 and CO_2 conversion increased with the rising of reaction temperature. However, the catalytic activity declined when reaction temperature reached 800 °C. This results are consistent with our previous research study [56]. Moreover, the CO_2 conversion was always higher, which was attributed to the RWGS reaction ($CO_2+H_2 \rightarrow CO + H_2O$). As evidenced in Fig. 6, the catalytic activity of Co/AC-N-650 is higher than Co/AC-N-850 and Co/AC-N-750. This might be related to the high ratio of Co^{2+} and more defective sites on catalysts. It has been suggested that the defective sites would favour the redox reaction, providing much more active sites in the catalyst and enhancing the electron transfer rate.

To further study the longevity of the catalysts, the CH_4 and CO_2 conversion as function of time were investigated to evaluate performance stability of DRM reaction over the catalysts. Fig. 7a and b shows the CH_4 and CO_2 conversion over Co/AC-N-650, Co/AC-N-750, and Co/AC-N-850, respectively. The initial conversion of CH_4 and CO_2 over three catalysts are unstable in the first 100 min, the CH_4 and CO_2 conversion of three catalysts could be observed to decrease with prolonging

reaction time. The decrease and increase of the activity may be attributed that a part of active metals poisoned by surface oxygen, due to the strong adsorption to oxygen species. However, the specific reasons for this phenomenon is unclear [57]. The experimental results indicate that all catalysts possessed high and same initial activity which decreased quickly with time. The reaction time was about 100 min, the catalytic activity reached the lowest level. There was a slowly increase in activity with time, after reaching a minimum. Although the conversions were lower than the initial values, the CH_4 and CO_2 conversion reached a stably state after the 600 min mark. For Co/AC-N-650, the CH_4 and CO_2 conversion were 59% and 73% respectively when the activity was stable. The CO_2 conversion rates of Co/AC-N-750 and Co/AC-N-850 were same but it was lower than Co/AC-N-650. The CO_2 conversion of three catalysts are higher than those of CH_4, which demonstrates that the reverse of WGSR reaction occurred simultaneously [58,59].

The TEM analysis was used to study the Co particle size distributions and particle size of fresh and spent catalysts. Fig. 8a–c and d-f shows the TEM micrographs of the fresh Co/
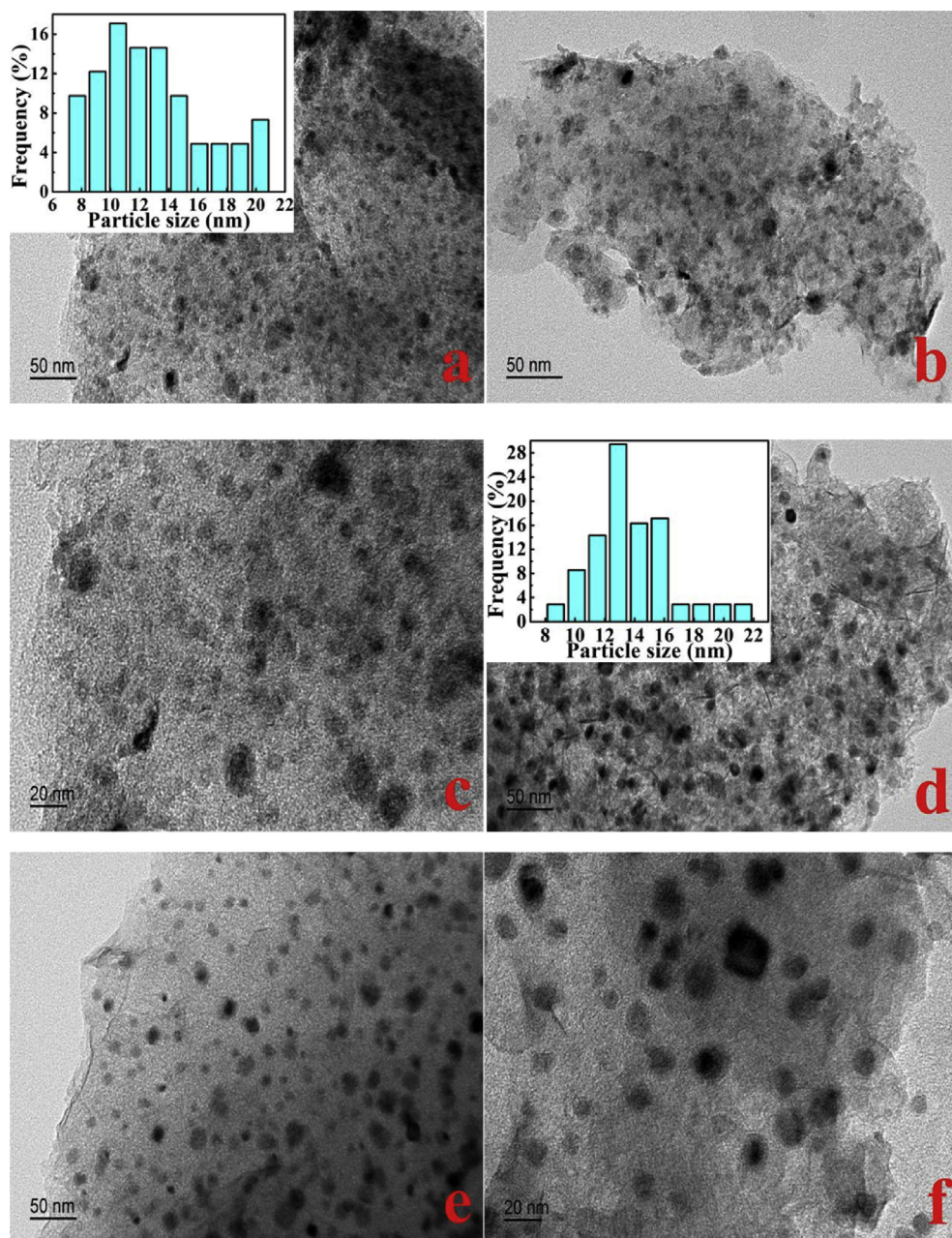
Fig. 8 – TEM images of the fresh (a–c) and used (d–f) Co/AC-N-650 catalysts.

AC-N-650 catalysts and used catalysts after 750 min reaction, respectively. The cobalt species particles size distributions of fresh and spent catalysts are also shown in Fig. 8a and d. As shown in Fig. 8a–c, the size of cobalt species particles was varied from 7 to 21 nm with an average particle size of about 12.82 nm. It demonstrated cobalt species were distributed uniformly on the surface of AC-N-650. Compared the TEM micrographs before and after the catalyst, the average particles size (13.7) of spent catalysts was found to increase slightly. Moreover, the diameter of most particles was in the range of 10–16 nm, it was indicated that the cobalt species were dispersed homogeneously over the surface of AC-N-650 and no agglomeration was occurred between particles after long DRM reaction.

Fig. 9 shows the nitrogen adsorption-desorption isotherms and pore size distribution of samples with different nitrogen content and without N-doped. As shown in Fig. 9a, all samples show a type I isotherm with a H4 hysteresis loop, indicating a high specific surface area. Compared with non-nitrogen doped catalysts, pore volume of N-doped catalysts decreased with the increase of melamine content. From Table 3 it can be seen that the doping amount of nitrogen has great influence on catalysts physical structure. The specific surface area of the catalysts decreased from 773.6 to 727.2 m^2/g when the addition of melamine increased from 4.43 to 13.3 g.

For comparison, other Co/AC-N-M were also prepared using different content of melamine. As shown in Fig. 10a, peaks centered at about 400 and 790 eV for all catalysts
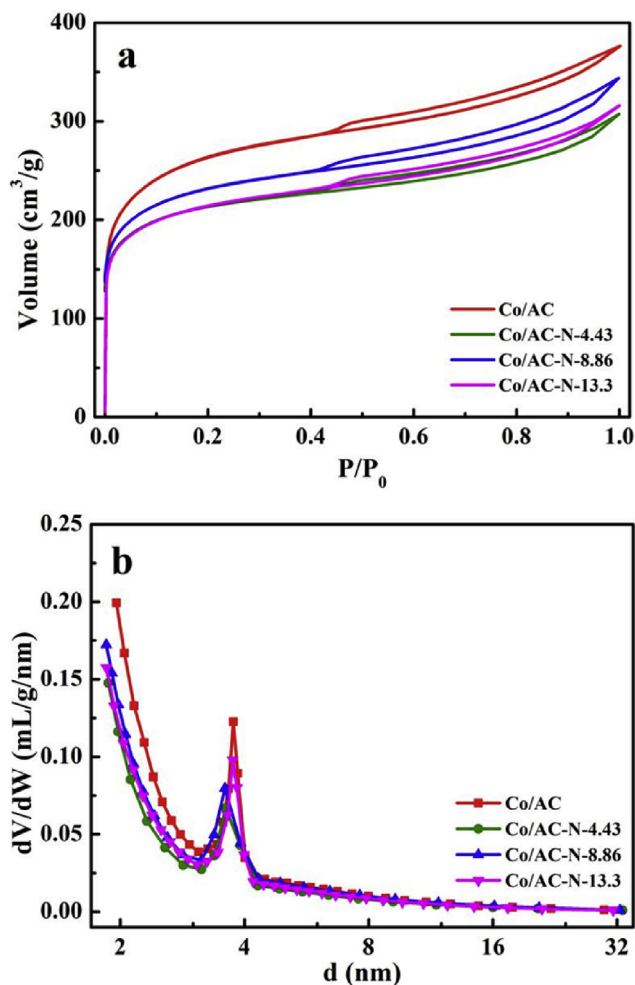
Fig. 9 — N₂-adsorption-desorption isotherms and pore size distribution of Co/AC, Co/AC-N-4.43, Co/AC-N-8.86 and Co/AC-N-13.3.

correspond to N1s and Co 2p, respectively. The doping levels of N increased with the increase of melamine addition. A small amounts of N element were detected for Co/AC catalysts, this mainly due to the existence of N-containing groups in coal-based activated carbon. The atomic ratios of three catalysts are shown in Table 4. As shown in Table 4, it can be seen that the content of O also increased with the increasing of nitrogen doping and highest content of Co was detected on
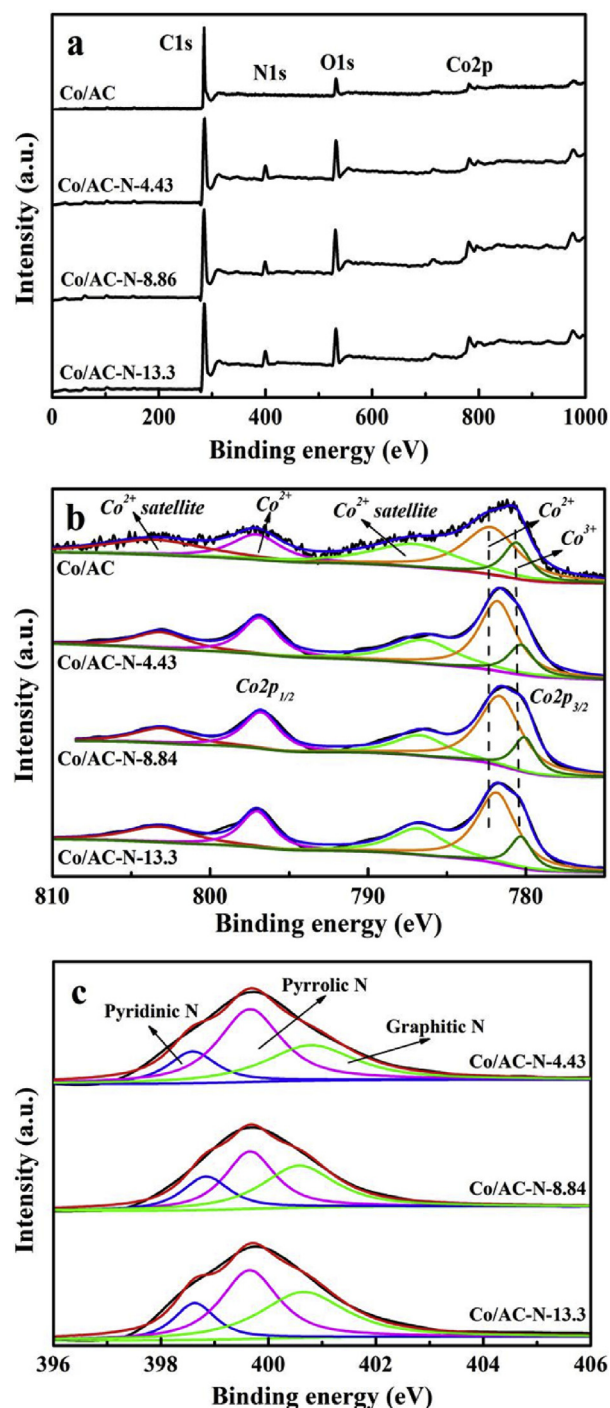

Fig. 10 — (a) XPS survey, (b) Co 2p scan and (c) N 1s scan of Co/AC, Co/AC-N-4.43, Co/AC-N-8.86, Co/AC-N-13.3.

Table 3 — Texture parameters of the samples.

Sample	N₂ adsorption over supports		
	BET surface area (m²/g)[a]	Average pore diameter (nm)[b]	Pore volume (cm³/g)[c]
Co/AC	956.9	2.54	0.61
Co/AC-N-4.43	773.6	2.63	0.46
Co/AC-N-6.68	764.2	2.71	0.53
Co/AC-N-13.3	727.2	2.69	0.49

[a] BET specific area.
[b] Total pore volumes were obtained at $P/P_0 = 0.99$.
[c] Average pore diameter calculated by BJH method.

Table 4 — Elemental contents of catalysts obtained by XPS.

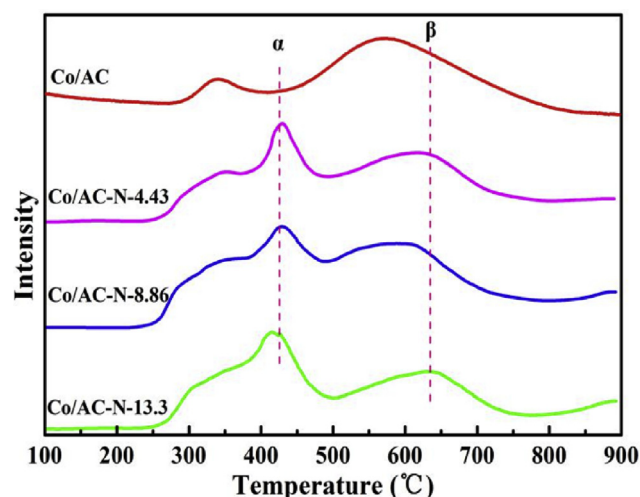| Catalyst	Element content/%			
	C	N	O	Co
Co/AC	84.60	1.62	10.16	1.62
Co/AC-N-4.43	75.71	8.21	13.80	1.29
Co/AC-N-6.68	75.20	6.86	14.70	2.13
Co/AC-N-13.3	74.28	8.61	14.78	2.23

Table 5 − XPS data of Co2p region for the Co/AC, Co/AC-N-4.43, Co/AC-N-8.86, Co/AC-N-13.3 catalysts.

| Catalyst	Binding energy Co $2p_{1/2}$ (eV)[a]			Binding energy Co $2p_{3/2}$ (eV)[a]			Co^{2+}/Co^{3+} (molar ratio)[b]	Co^{2+} satellite/Co^{3+} (molar ratio)[b]
	Co^{2+} satellite	Co^{2+}	Co^{3+}	Co^{2+} satellite	Co^{2+}	Co^{3+}		
Co/AC	803.42(3186)	797.05(2608)	795.0(0)	787.04(4126)	782.19(5351)	780.58(1971)	4.03	3.71
Co/AC-N-4.43	803.109(3269)	796.85(4917)	794.6(0)	786.47(5509)	781.78(9503)	780.29(2817)	5.12	3.12
Co/AC-N-8.86	803.06(4937)	796.75(7866)	794.3(0)	786.67(6489)	781.63(17758)	780.06(4900)	5.22	2.33
Co/AC-N-13.3	803.18(5424)	797.02(6216)	794.6(0)	786.79(7288)	781.85(14451)	780.30(3629)	5.69	3.50

[a] The peak area of different cobalt species.
[b] The molar ratio of Co^{2+}/Co^{3+} and Co^{2+} satellite/Co^{3+} was calculated from peak area in Fig. 8b.

Co/AC-N-13.3 catalyst by XPS analysis, this result is in consistent with the result that highest content of O on Co/AC-N-13.3. The characterization results have shown that the chemical compositions of catalysts were changed by doping N atoms in the Co-based catalysts. The Co 2p spectra of four catalysts are shown in Fig. 10b and the corresponding data are listed in Table 5. As shown in Fig. 4b, the experimental results were deconvoluted by six peaks, which correspond to the Co^{2+} satellite, Co^{2+} and Co^{3+}. The Co^{3+} species were still not detected for Co $2p_{3/2}$ in all catalysts. The surface atomic ratios are shown in Table 5. It could be observed that Co^{2+}/Co^{3+} and Co^{2+} satellite/Co^{3+} ratios increased with the increase of melamine addition. That the doping of N enhances the catalytic reducibility. H_2-TPR analysis results of the calcinated Co/AC, Co/AC-N-4.43, Co/AC-N-8.86, Co/AC-N-13.3 catalysts is presented in Fig. 11. It can be seen that two main peaks (peak α and peak β) is found for all N-doped and undoped catalysts. For undped catalyst Co/AC, small peak centered around 350 °C was detected, which contributed to the reduction of high dispersion Co_3O_4, the peak at 370 °C could be attributed to the reduction of CoO. Compared with undoped catalysts, peak β shifted to the higher temperatures for all N-doped catalysts, due to the higher interaction between active metals and supports. Moreover, the intensity of peak β for N-doped catalysts increased, which indicated that more active species was loaded on the modified and higher dispersity was achieved on these catalysts.

Fig. 12 shows the conversions of CH_4 and CO_2 on Co/AC, Co/AC-N-4.43, Co/AC-N-8.86 and Co/AC-N-13.3 at different reaction temperature. Each temperature interval was sustained for 30 min until the catalyst bed temperature was stable. The CH_4 and CO_2 conversions were obtained on the basis of average values. The CH_4 conversion of all catalyst (Fig. 12a) shows that the highest conversion is achieved by Co/AC-N-13.3. The lowest conversion of CH_4 is displayed by Co/AC, the sample without N doping of the. It is obvious that the conversion of CO_2 was higher than that of CH_4 for four

Fig. 11 − H_2-TPR profiles of Co/AC, Co/AC-N-4.43, Co/AC-N-8.86, Co/AC-N-13.3.
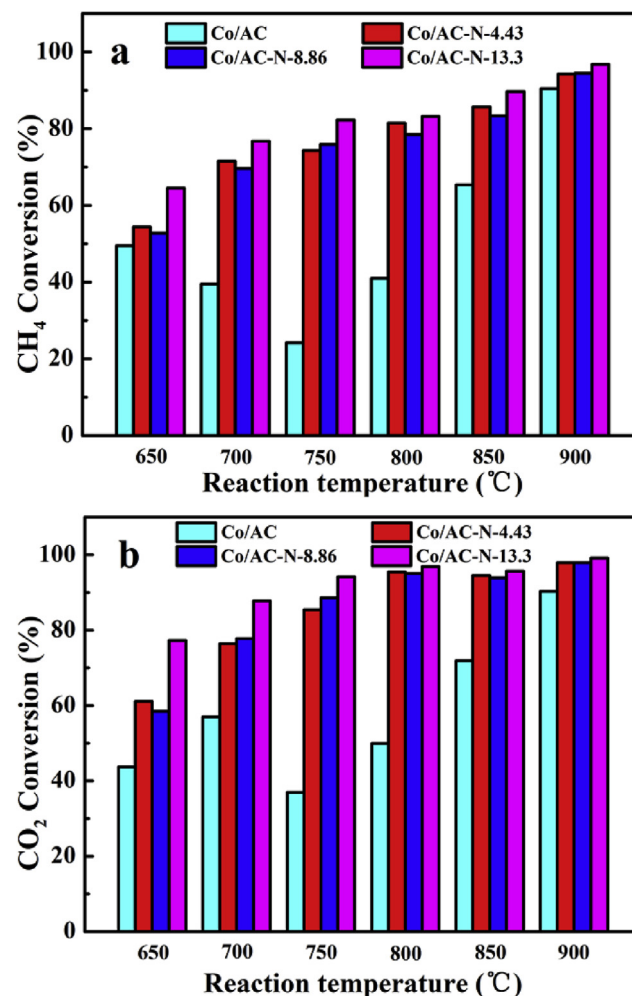
Fig. 12 − CH_4 (a) and CO_2 (b) conversion of Co/AC, Co/AC-N-4.43, Co/AC-N-8.86, Co/AC-N-13.3 at different reaction temperature.

catalysts due to the occurring of RWGS reaction. For all N-doped catalysts, it was observed that CH_4 and CO_2 conversions increased with the increase in reaction temperature because of the characteristics of endothermic for DRM reaction. Moreover, the modification of has great influence on catalytic activity when the reaction temperature was below 900 °C.

To investigate the stability of Co/AC-N-M catalysts, the DRM reaction was conducted at 800 °C. The conversions of CH_4 and CO_2 of Co/AC-N-M catalysts are shown in Fig. 13. For all catalysts, the initial CH_4 and CO_2 conversions were basically same, the conversion of CO_2 was higher than CH_4 due to the RWGS reaction. All catalysts deactivated rapidly after 100 min and than the catalytic activity increased and kept stable after 650 min. This could be attributed to the catalyst reconstruction during DRM reaction. Compared with un-modified catalyst, the catalytic performance had varying degrees of improve after nitrogen doping. Among all catalysts, Co/AC-N-13.3 has the highest performance, CH_4 and CO_2 conversions reached 59% and 73% respectively after 740 min reaction. Despite a high surface area, Co/AC had lowest

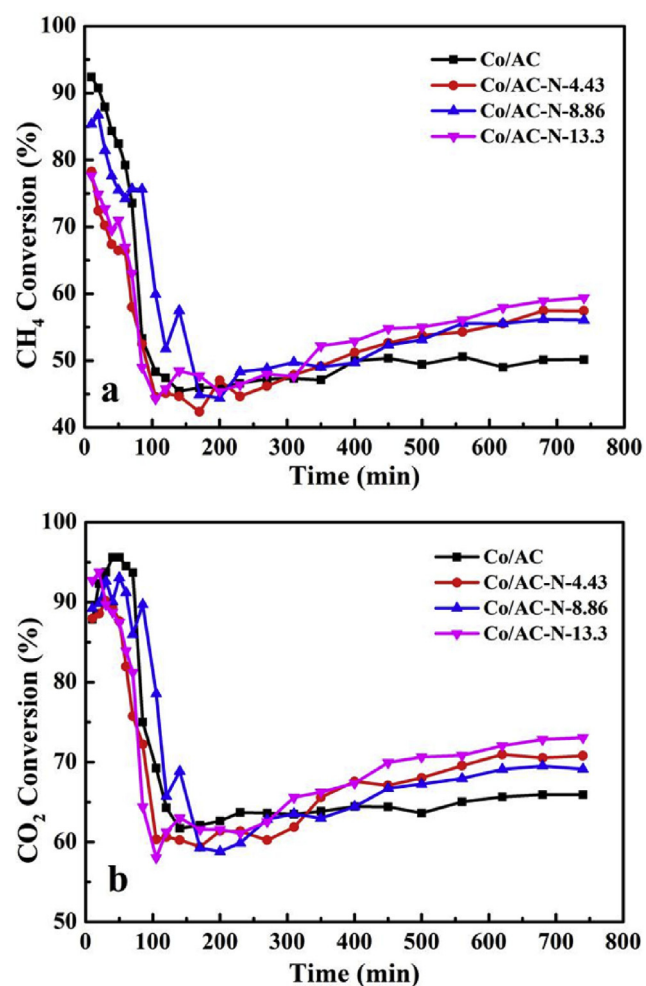catalytic performance with CH_4 and CO_2 conversions of 50.16% and 65.94 respectively. The catalytic activity order of four catalysts for DRM reaction is Co/AC-N-13.3 ˃ Co/AC-N-4.43 ˃ Co/AC-N-8.86 ˃ Co/AC. It was obvious that chemical property of the has significantly influenced on the catalytic performance of catalysts.

Conclusions

Nitrogen doped activated carbon cobalt catalyst was prepared by impregnation method for DRM reaction. The nitrogen doping could remarkably improve the catalyst performance. Characterization results indicated that N introduction improved the oxidation-reduction ability, increased the molar ratio of Co^{2+}/Co^{3+} and the interaction between active metal and, which are facilitated for the enhancement of DRM activity. Moreover, a series of different calcination temperature and nitrogen doping catalysts were prepared. The results demonstrated that preparation conditions of N-doped carbon material had different effect on the performance of Co/AC-N catalysts. By comparing the catalytic activities of the catalysts with different calcination temperature and nitrogen doping catalysts, it was concluded that highest catalytic activity was achieved on the catalyst, which the calcination temperature was 650 °C and the amount of nitrogen doping was 13.3 g. Highest Co^{2+}/Co^{3+} molar ratio and most surface defects were obtained on this catalyst.

Fig. 13 — Stability tests at 800 °C: CH_4 (a) and CO_2 (b) conversion over catalysts with different nitrogen doping. Reaction conditions: CH_4/CO_2 = 1:1, total flow rate = 120 mL/min, 1 atm.

REFERENCES

[1] Abasaeed AE, Al-Fatesh AS, Naeem MA, Ibrahim AA, Fakeeha AH. Catalytic performance of CeO_2 and ZrO_2 supported Co catalysts for hydrogen production via dry reforming of methane. Int J Hydrogen Energy 2015;40:6818—26.
[2] Özkara-Aydınoğlu Ş, Özensoy E, Aksoylu AE. The effect of impregnation strategy on methane dry reforming activity of Ce promoted Pt/ZrO_2. Int J Hydrogen Energy 2009;34:9711—22.
[3] Kumar N, Kanitkar S, Wang Z, Haynes D, Shekhawat D, Spivery JJ. Dry reforming of methane with isotopic gas mixture over Ni-based pyrochlore catalyst. Int J Hydrogen Energy 2019;44:4167—76.
[4] Xie H, Yu Q, Zhang Y, Zhang J, Liu J, Qin Q. New process for hydrogen production from raw coke oven gas via sorption-enhanced steam reforming: thermodynamic analysis. Int J Hydrogen Energy 2017;42:2914—23.
[5] Steen EV, Schulz H. Polymerisation kinetics of the Fischer-Tropsch CO hydrogenation using iron and cobalt based catalysts. Appl Catal Gen 1999;186:309—20.

[6] Zhang G, Hao L, Yong J, Du Y, Zhang Y. CO_2 reforming of CH_4 over efficient bimetallic Co-Zr/AC catalyst for H_2 production. Int J Hydrogen Energy 2015;40:12868—79.

[7] Ayodele BV, Khan MR, Su SL, Cheng CK. Production of CO-rich hydrogen from methane dry reforming over lanthania-supported cobalt catalyst: kinetic and mechanistic studies. Int J Hydrogen Energy 2016;41:4603—15.

[8] Zhao B, Yan B, Yao S, Xie Z, Wu Q, Ran R, et al. $LaFe_{0.9}Ni_{0.1}O_3$ perovskite catalyst with enhanced activity and coke-resistance for dry reforming of ethane. J Catal 2018;358:168—78.

[9] Bouarab R, Akdim O, Auroux A, Cherifi O, Mirodatos C. Effect of MgO additive on catalytic properties of Co/SiO_2 in the dry reforming of methane. Appl Catal Gen 2005;264:161—8.

[10] Aider N, Touahra F, Bali F, Djebarri B, Lerari D, Bachari K, et al. Improvement of catalytic stability and carbon resistance in the process of CO_2 reforming of methane by CoAl and CoFe hydrotalciet-derived catalyts. Int J Hydrogen Energy 2018;43:8256—66.

[11] Omoregbe O, Danh HT, Nguyen-Huy C, Setiabudi HD, Abidin SZ, Truong QD, et al. Syngas production from methane dry reforming over Ni/SBA-15 catalyst: effect of operating parameters. Int J Hydrogen Energy 2017;42:11283—94.

[12] Tsoukalou A, Imtiaz Q, Kim SM, Abdala PM, Yoon S, Müller CR. Dry-reforming of methane over bimetallic Ni-M/La_2O_3 (M = Co, Fe): the effect of the rate of $La_2O_2CO_3$ formation and phase stability on the catalytic activity and stability. J Catal 2016;343:208—14.

[13] Karemore AL, Vaidya PD, Sinha R, Chugh P. On the dry and mixed reforming of methane over Ni/Al_2O_3-Influence of reaction variables on syngas production. Int J Hydrogen Energy 2016;41:22963—75.

[14] Li Z, Min L, Bian Z, Kathiraser Y, Kawi S. Design of highly stable and selective core/yolk-shell nanocatalysts-A review. Appl Catal B Environ 2016;188:324—41.

[15] Li Z, Wang Z, Kawi S. Sintering and coke resistant core/yolk shell catalyst for hydrocarbon reforming. ChemCatChem 2019;11:202—24.

[16] Li Z, Kawi S. Multi-Ni@Ni phyllosilicate hollow sphere for CO_2 reforming of CH_4: influence of Ni precursors on structure, sintering, and carbon resistance. Catal Sci Technol 2018;8:1915—22.

[17] Wigmans T, Elfring R, Moulijn JA. On the mechanism of the potassium carbonate catalysed gasification of activated carbon: the influence of the catalyst concentration on the reactivity and selectivity at low steam pressures. Carbon 1983;21:1—12.

[18] Zhu J, Carabineiro SAC, Shan D, Faria JL, Zhu Y, Figueiredo JL. Oxygen activation sites in gold and iron catalysts supported on carbon nitride and activated carbon. J Catal 2010;274:207—14.

[19] Villa A, Wang D, Dimitratos N, Su D, Trevisan V, Prati L. Pd on carbon nanotubes for liquid phase alcohol oxidation. Catal Today 2010;150:8—15.

[20] Rajalakshmi N, Ryu H, Shaijumon MM, Ramaprabhu S. Performance of polymer electrolyte membrane fuel cells with carbon nanotubes as oxygen reduction catalyst support material. J Power Sources 2005;140:250—7.

[21] Jarrah NA, Ommen JGV, Lefferts L. Mechanistic aspects of the formation of carbon-nanofibers on the surface of Ni foam: a new microstructured catalyst support. J Catal 2006;239:460—9.

[22] Chinthaginjala JK, Seshan K, Lefferts L. Preparation and application of carbon-nanofiber based microstructured materials as catalyst supports. Ind Eng Chem Res 2007;46:3968—78.

[23] Guo D, Han S, Ma R, Zhou Y, Liu Q, Wang J, et al. In situ formation of iron-cobalt sulfides embedded in N, S-doped mesoporous carbon as efficient electrocatalysts for oxygen reduction reaction. Microporous Mesoporous Mater 2018;270:1—9.

[24] Chen L, Xu C, Yang L, Zhou M, He B, Chen Z, et al. Nitrogen-doped holey carbon nanotubes: dual polysulfides trapping effect towards enhanced lithium-sulfur battery performance. Appl Surf Sci 2018;454:284—94.

[25] Yin X, Sun W, Lv LP, Wang Y. Boosting lithium-ion storage performance by synergistically coupling $Zn_{0.76}Co_{0.24}S$ with N-/S-doped carbon and carbon nanofiber. Chem Eng J 2018;346:376—87.

[26] Feng LL, Zou Y, Li C, Gao S, Zhou LJ, Sun Q, et al. Nanoporous sulfur-doped graphitic carbon nitride microrods: a durable catalyst for visible-light-driven H_2 evolution. Int J Hydrogen Energy 2014;39:15373—9.

[27] Johansson AC, Larsen JV, Verheijen MA, Haugshøj KB, Clausen HF, Kessels WMM, Christensen LH, Thomsen EV. Electrocatalytic activity of atomic layer deposited Pt-Ru catalysts onto N-doped carbon nanotubes. J Catal 2014;311:481—6.

[28] Yong JC, Han SK, Im H, Myung Y, Jung GB, Chi WL, et al. Nitrogen-doped graphitic layers deposited on silicon nanowires for efficient lithium-ion battery anodes. J Phys Chem C 2013;115:9451—7.

[29] Qu H, Zhang X, Zhan J, Sun W, Si Z, Chen H. Biomass-based nitrogen-doped hollow carbon nanospheres derived directly from glucose and glucosamine: structural evolution and supercapacitor properties. Acs Sustain Chem Eng 2018;6:7380—9.

[30] Yu J, Guo M, Muhammad F, Wang A, Yu G, Ma H, et al. Simple fabrication of an ordered nitrogen-doped mesoporous carbon with resorcinol-melamine-formaldehyde resin. Microporous Mesoporous Mater 2014;190:117—27.

[31] Wang H, Wang W, Gui M, Asif M, Wang Z, Yu Y, et al. Uniform Fe_3O_4/nitrogen-doped mesoporous carbon spheres derived from ferric citrate-bonded melamine resin as an efficient synergistic catalyst for oxygen reduction. ACS Appl Mater Interfaces 2017;9:335—44.

[32] Yang Y, Zhang J, Zhuang J, Wang X. Synthesis of nitrogen-doped carbon nanostructures from polyurethane sponge for bioimaging and catalysis. Nanoscale 2015;7:12284—90.

[33] Xiao S, Liu S, Zhang J, Wang Y. Polyurethane-derived N-doped porous carbon with interconnected sheet-like structure as polysulfide reservoir for lithium-sulfur batteries. J Power Sources 2015;293:119—26.

[34] Ning X, Liu Z, Hu A, Tang Q, Fan B, Zhang S, et al. In-situ construction of interconnected N-doped porous carbon-carbon nanotubes networks derived from melamine anchored with MoS_2 for high performance lithium-ion batteries. J Alloy Comp 2018;744:75—81.

[35] Sun X, Zhang W, Tang D, Qiao ZA, Liu Y, Liang D, et al. Co-entrapped, N-doped mesoporous carbons prepared from melamine formaldehyde resins with $CoCl_2$ as template for hydrogen evolution. J Colloid Interface Sci 2018;516:416—22.

[36] Horikawa T, Sakao N, Sekida T, Hayashi JI, Do DD, Katoh M. Preparation of nitrogen-doped porous carbon by ammonia gas treatment and the effects of N-doping on water adsorption. Carbon 2012;50:1833—42.

[37] Wang Y, Liu H, Wang K, Song S, Tsiakaras P. 3D interconnected hierarchically porous N-doped carbon with NH_3 activation for efficient oxygen reduction reaction. Appl Catal B Environ 2017;210:57—66.

[38] Zou K, Deng Y, Chen J, Qian Y, Yang Y, Li Y, et al. Hierarchically porous nitrogen-doped carbon derived from the activation of agriculture waste by potassium hydroxide

and urea for high-performance supercapacitors. J Power Sources 2018;378:579—88.

[39] Wang K, Xu M, Gu Y, Gu Z, Fan QH. Symmetric supercapacitors using urea-modified lignin derived N-doped porous carbon as electrode materials in liquid and solid electrolytes. J Power Sources 2016;332:180—6.

[40] Wang X, Tang Y, Shi P, Fan J, Xu Q, Min Y. Self-evaporating from inside to outside to construct cobalt oxide nanoparticles-embedded nitrogen-doped porous carbon nanofibers for high-performance lithium ion batteries. Chem Eng J 2018;334:1642—9.

[41] Zhong ME, Guan J, Feng Q, Wu X, Xiao Z, Zhang W, et al. Accelerated polysulfide redox kinetics revealed by ternary sandwich-type S@Co/N-doped carbon nanosheet for high-performance lithium-sulfur batteries. Carbon 2018;128:86—96.

[42] Su C, Pei C, Wu B, Qian J, Tan Y. Highly doped carbon nanobelts with ultrahigh nitrogen content as high-performance supercapacitor materials. Small 2017;13(29):1700834.

[43] Amir O, Kalish R. Properties of nitrogen-doped amorphous hydrogenated carbon films. J Appl Phys 1991;70:4958—62.

[44] Wang H, Maiyalagan T, Wang X. Review on recent progress in nitrogen-doped graphene: synthesis, characterization, and its potential applications. ACS Catal 2012;2:781—94.

[45] Ying X, Mo Y, Jing T, Ping W, Yu H, Yu J. The synergistic effect of graphitic N and pyrrolic N for the enhanced photocatalytic performance of nitrogen-doped graphene/TiO_2 nanocomposites. Appl Catal B Environ 2016;181:810—7.

[46] Jia Q, Ramaswamy N, Tylus U, Strickland K, Li J, Serov A, et al. Spectroscopic insights into the nature of active sites in iron-nitrogen-carbon electrocatalysts for oxygen reduction in acid. Nanomater Energy 2016;29:65—82.

[47] Liu Z, Jing Y, Li X, Zhang L, Dong L, Liu X, et al. Facile synthesis of N-doped carbon layer encapsulated Fe_2N as an efficient catalyst for oxygen reduction reaction. Carbon 2017;127:636—42.

[48] Liu H, Zhang Y, Li R, Sun X, Désilets S, Abou-Rachid H, et al. Structural and morphological control of aligned nitrogen-doped carbon nanotubes. Carbon 2010;48:1498—507.

[49] Li Z, Li M, Jangam A, Kawi S. NiCo@NiCo phyllosilicate@CeO_2 hollow core shell catalysts for steam reforming of toluene as biomass tar model compound. Energy Convers Manag 2019;180:822—30.

[50] Sharma BK, Sharma MP, Kumar S, Roy SK, Roy SK, Badrinarayanan S, et al. Studies on cobalt-based Fischer-Tropsch catalyst and characterization using SEM and XPS techniques. Appl Catal Gen 2001;211:203—11.

[51] Liu ZQ, Cheng H, Li N, Ma TY, Su YZ. $ZnCo_2O_4$ quantum dots anchored on nitrogen-doped carbon nanotubes as reversible oxygen reduction/evolution electrocatalysts. Adv Mater 2016;28:3777—84.

[52] Zaman M, Khodadi A, Mortazavi Y. Fischer-Tropsch synthesis over cobalt dispersed on carbon nanotubes-based supports and activated carbon. Fuel Process Technol 2009;90:1214—9.

[53] Bao T, Zhao Z, Dai Y, Lin X, Jin R, Wang G, et al. Supported Co_3O_4-CeO_2 catalysts on modified activated carbon for CO preferential oxidation in H_2-rich gases. Appl Catal B Environ 2012;119—120:62—73.

[54] Li Z, Wang Z, Bo J, Kawi S. Sintering resistant Ni nanoparticles exclusively confined within SiO_2 nanotubes for CH_4 dry reforming. Catal Sci Technol 2018;8:3363—71.

[55] Santos MDS, Neto RCR, Noronha FB, Bargiela P, Rocha MDGCD, Resini C, et al. Perovskite as catalyst precursors in the partial oxidation of methane: the effect of cobalt, nickel and pretreatment. Catal Today 2017;299:229—41.

[56] Sun Y, Zhang G, Liu J, Zhao P, Peng H, Ying X, et al. Effect of different activated carbon support on CH_4-CO_2 reforming over Co-based catalysts. Int J Hydrogen Energy 2018;43:1497—507.

[57] Bian Z, Das S, Wai MH, Hongmanorom P, Kawi S. A review on bimetallic Ni-Based catalysts for CO_2 reforming of methane. ChemPhysChem 2017;18:3117—34.

[58] Foppa L, Silaghi MC, Larmier K, Comas-Vives A. Intrinsic reactivity of Ni, Pd and Pt surfaces in dry reforming and competitive reactions: insights from first principles calculations and microkinetic modeling simulations. J Catal 2016;343:196—207.

[59] Fouskas A, Kollia M, Kambolis A, Papadopoulou C, Matralis H. Boron-modified Ni/Al_2O_3 catalysts for reduced carbon deposition during dry reforming of methane. Appl Catal Gen 2014;474:125—34.